

# A gray-scale mapping method to consider locally varying properties for wood forming simulations

Christian Liebold<sup>1</sup>, David Zerst<sup>2</sup>, Thomas Gereke<sup>3</sup>, Sebastian Clauß<sup>4</sup>

<sup>1</sup>DYNAmore GmbH

<sup>2</sup>German Aerospace Center

<sup>3</sup>ITM, TU Dresden

<sup>4</sup>Mercedes Benz AG

**Keywords:** *finite element mapping, veneer laminates, interior design*

## 1 Abstract

Automotive interior components in upper-class vehicles are often made of wood veneer sheets that are subject to a forming process [1]. Due to the anisotropy and inhomogeneity of the material caused by the development of annual rings during the growth of the tree, establishing a stable production process based on trial-and-error forming tests is time-consuming and costly [2]. Hence, numerical methods for simulating the forming process are in high demand to support the development of feasible trim part geometries. The key for reliable process simulations of wood-based materials is the consideration of the variability of material properties.

In this paper, the authors present a method to account for the locally varying properties of early and late wood in finite element simulations using a gray-scale mapping procedure. The method was introduced in [3] and was implemented in the software tool Envyo® [5]. The developed approach, which consists of a gravity loading step and a forming simulation with `*MAT_LAMINATED_COMPOSITE_FABRIC` (`*MAT_58`) in LS-DYNA [4], is validated using the example of a palm rest of the Mercedes-Benz X167 series. Furthermore, the necessary steps and assumptions for material data calibration are demonstrated.

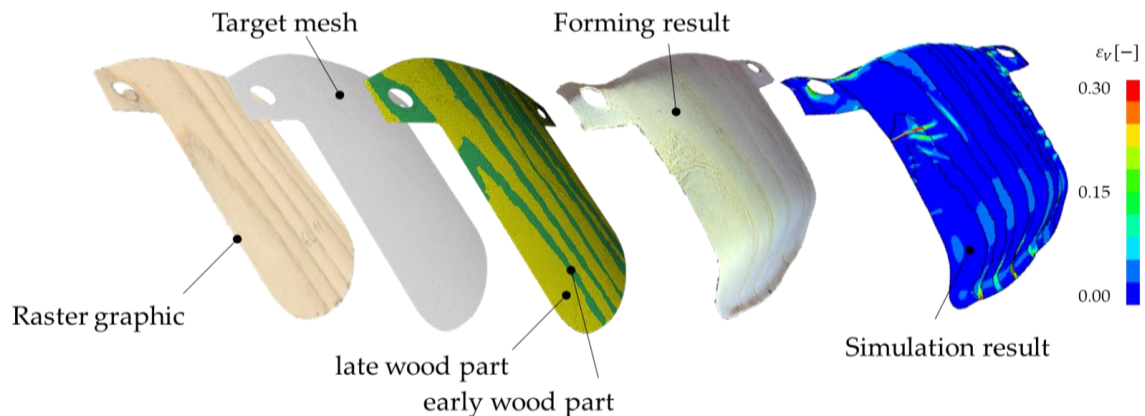


Fig. 1: Illustration of the established process chain.

## 2 Introduction

Veneer laminates used for 3D-formed surfaces of automotive interior parts are manufactured of a veneer sheet bonded to a non-woven fabric using a phenolic resin [3]. Different cutting techniques to create the wood veneer layer such as rotary or plain slicing methods exist [6] resulting in different patterns of the early- and late wood areas and therefore inhomogeneous material properties. Due to the nature of the material, the shape, size and density of the annual rings depend on the environmental growth conditions and the tree species used. Therefore, each specimen or manufactured component is unique, making it an aesthetically pleasing material for the interiors of high-end vehicles, but challenging for estimating formability when it comes to serial production. Fig. 2 illustrates a plain slicing cutting technique that

produces different patterns depending on the position of the cutout. A picture taken from a microscope [3] illustrates the composition of the veneer laminate.

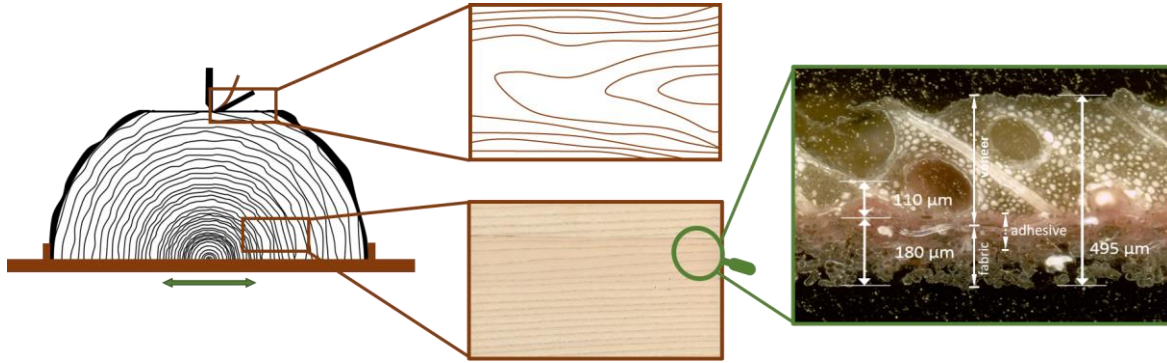


Fig. 2: Illustration of the cutting process of veneer layers (left), the resulting patterns and typical areas of failure (middle), and a microscopic view on the laminate [3].

Due to the mentioned inhomogeneities of the material, the focus of this work is to introduce local varying material properties of early and late wood into the finite element (FE) model, allowing for a better prediction of the formability. Using a clustering algorithm based on a gray-scale mapping method, areas of early and late wood can be assigned to different parts in the FE model, allowing different material properties to be considered using LS-DYNA's `*MAT_58`. The material properties used for the simulation were calibrated based on tensile, shear, and Nakajima tests. Unknown material properties were estimated from literature [2]. Furthermore, the distribution of both, experimental scatter and correlating simulation results of wood specimen were studied. Finally, the modelling approach was validated in forming simulations of an automotive part from a running series production.

### 3 Experimental testing

In this study, ash wood was selected, which is commonly used for parts of vehicle interiors. To reduce modeling and testing, only the composite response was studied in this work. Experimental testing was carried out under normal conditions (20°C, 65% relative humidity) and after water-immersion to represent the forming conditions. As shown in [7], formability of the material is increased with a higher degree of moisture. The moisture content resulting from the water immersion was about 52%. For comparison: Under normal conditions, the moisture content was about 7%.

#### 3.1 Tensile tests

Tensile testing was done based on the work of [8], with a specimen size of 120 x 10 mm<sup>2</sup> and a measuring range of 80 x 10 mm<sup>2</sup>. Table 1 depicts the Young's moduli  $E_{ii}$ , maximum strengths  $\sigma_{max,ii}$ , and corresponding strains  $\epsilon_{max,ii}$  based on the relative moisture content for a loading direction along (refers to the 11-direction) and perpendicular (refers to the 22-direction) to the wood fibers. Specimens tested under normal conditions are referred to as *dry*, while specimens with higher moisture content are referred to as *wet*. In summary, increasing the moisture content significantly increases the maximum strains at failure for both longitudinal and transverse loading directions. The maximum strength is almost the same for the direction perpendicular to the main fiber direction and reduced for the fiber direction. The significant reduction in stiffness for the 22-direction when applying water to the specimen also explains the above-mentioned increase in formability of the material. In total, 10 specimens were tested for each loading direction. Table 1 therefore provides the mean values.

Table 1: Measured material properties in tensile tests depending on material direction and moisture content.

	$E_{11}$ [MPa]	$E_{22}$ [MPa]	$\sigma_{max,11}$ [MPa]	$\sigma_{max,22}$ [MPa]	$\epsilon_{max,11}$ [-]	$\epsilon_{max,22}$ [-]
<i>dry</i> :	6450	1760	63	13	0.0105	0.010
<i>wet</i> :	3540	380	40	12	0.0205	0.0626

As expected, specimens loaded in the 22-direction break along the fiber direction and between zones of early and late wood, or perpendicular to the loading direction. Specimens loaded along the direction

of the fibers also break perpendicular to the loading direction. The crack path is therefore rather random and not aligned with any material zones, as shown in Fig. 3.



Fig. 3: Crack pattern of tensile specimen loaded along the fiber main direction (11-direction) (top) and perpendicular to the fiber direction (22-direction) (bottom).

### 3.2 Shear tests

To determine the shear characteristics of the material, 20 picture frame tests, as described in [9], were performed for both, wet and dry specimens. The specimen size was chosen to be 10 mm. With reference to Fig. 4, the resulting shear angle is calculated from the changes in length of the diagonals of the specimen:

$$\gamma_{12} = \frac{|\Delta l_1| + |\Delta l_2|}{1 + |\Delta l_1| - |\Delta l_2|} \quad (1)$$

Shear stresses are calculated directly from the forces measured by the testing machine. Fig. 4 also shows the results of the finite element model – to the left, the resulting shear stresses, and to the right the resulting shear angles.

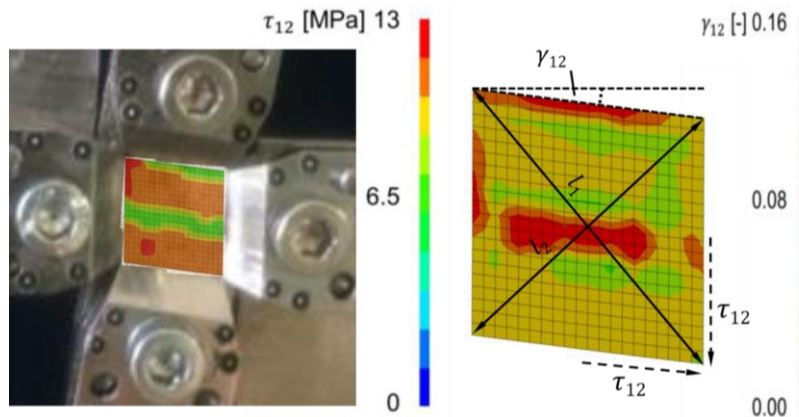


Fig.4: Picture frame test and resulting finite element results for the shear stresses (left) and the shear angle (right).

The resulting material properties, namely the shear stiffness  $G_{12}$ , the maximum shear strength  $\tau_{max,12}$ , and the corresponding maximum shear strain  $\gamma_{max,12}$  for dry and wet specimens are provided in Table 2. It should be noted that the wet specimens reached the maximum allowable shear angle of the machine, so that the properties for strength and strain are given with a “greater than/equal to” sign to account for the unknown properties beyond this point. Again, maximum shear strain increases with moisture content while shear modulus and shear strength decrease with increasing moisture content.

Table 2: Measured material properties in shear tests depending on material direction and moisture content.

	$G_{12}$ [MPa]	$\tau_{max,12}$ [MPa]	$\gamma_{max,12}$ [-]
<b>dry:</b>	900	24	0.07
<b>wet:</b>	270	$\geq 10$	$\geq 0.12$

### 3.3 Nakajima tests

To determine the formability of the veneer laminates, Nakajima tests were performed with different web widths of 30 mm, 70 mm, 125 mm, and full-circle samples according to [10]. A hemispherical punch deforms the circumferentially clamped blanks until fracture. A deformation limit diagram could not be determined from these tests due to the very low strains in the fiber direction. Nevertheless, they are useful for evaluating and recalibrating the material cards derived from the tensile and shear test procedures before proceeding to the component simulations. Furthermore, optical measurements using a GOM Aramis system were performed allowing for the evaluation of strain in both early and late wood zones. Fig. 5 exemplarily shows the final failure pattern of a specimen with a web width of 30 mm. Strain concentration is clearly visible in the areas of the early wood, which can be explained by the chemical and physical properties of its microstructure.

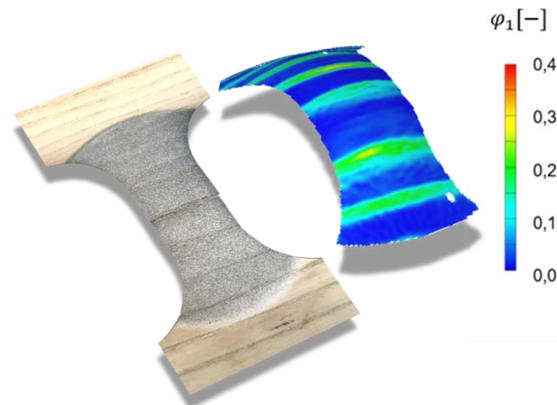


Fig. 5: Final failure pattern of a Nakajima test with a web width of 30 mm (left) and GOM strain measurement result (right).

## 4 Numerical modeling

In the following, the chosen modeling technique is introduced. First, an introduction to the gray-scale mapping technique is given, followed by a short overview on the applied material model and the resulting calibrated material properties. The gray-scale mapping technique was applied for material calibration, allowing for a differentiation between early and late wood zones. Finally, a stochastic investigation of ash wood in experimental testing and numerical analysis is presented.

### 4.1 Mapping and gray value analysis

As already presented in [1], [2], and [15], a gray-scale mapping routine was implemented into the mapping tool Envyo. It is based on a closest point search and a bucket-sort algorithm for speed-up. Images taken from the wood samples must first be transferred from a color image into a gray-scale image, e.g., using the freely available software GIMP. The gray-scale images must then be written to an ASCII \*.pgm (portable gray map) file, containing the gray-scale value of each pixel and the total number of pixels as *length* x *width*. A value of zero means completely black, while a value of 255 means white. Values in between indicate a gray value from dark to light gray. Envyo then reads and interprets the \*.pgm file. Therefore, the user needs to provide the size of the area covered by the pixel listed in the \*.pgm file such that the position is calculated in global coordinates. Point generation starts at the origin (0,0) and progresses along the x- and y- axis of the global coordinate system. Each generated point contains the information of its specific gray value. In addition to input and output file names and image size, users can specify information to transform the generated point cloud to fit the finite element target mesh and allow for proper data transfer. Part-IDs and therefore different material cards can be assigned to the finite element target mesh by providing ranges of gray-scale values to the mapping command file and the part number to be assigned. As already shown in Fig. 1, areas of early wood appear to have higher gray-scale values, meaning that they are darker compared to the late wood of an image taken from an ash wood specimen. In this work, a standard Gaussian filter was used to reduce unwanted peaks in the gray-scale image (see Fig. 6) and the gray-scale value was calibrated in a way that the

width of the early and late wood zones in the finite element mesh corresponded to the ones observed in the image. This calibration was performed qualitatively.

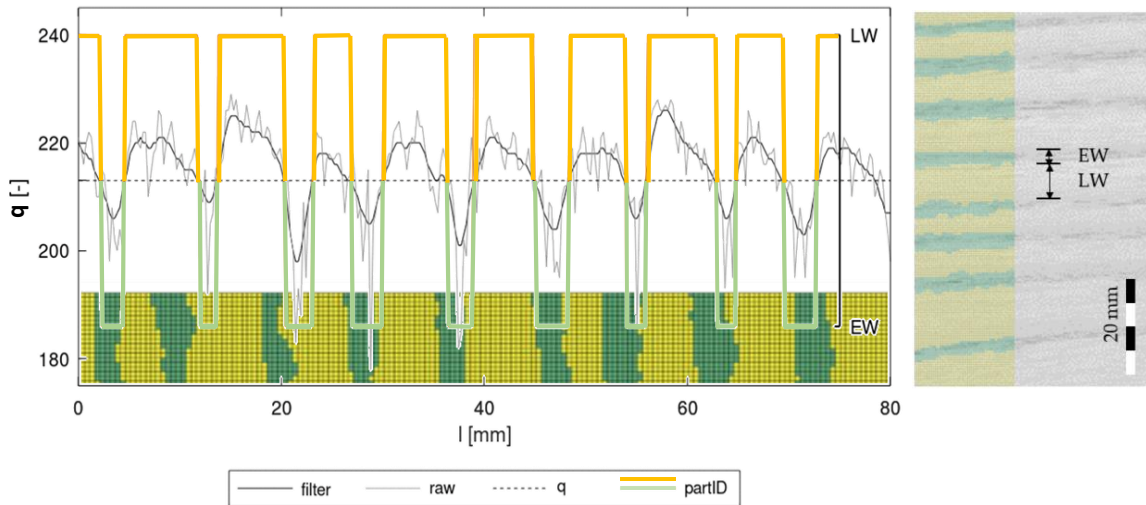


Fig. 6: Illustration of the gray-scale mapping method with filtered gray-scale values along the specimen main axis (left) and quantitative evaluation of the resulting mesh with clustered part-IDs (right).

## 4.2 Material calibration

For the numerical modeling of the early and late wood zones, **\*MAT\_LAMINATED\_COMPOSITE\_FABRIC** (**\*MAT\_58**) was chosen. A detailed description of the implementation based on the work of [11] can be found in [12]. A basic illustration of the general behavior of this material model is provided in Fig. 7. The figure also includes ratios for parameters in compressive loading, which could not be defined with the chosen testing scheme and are therefore defined based on literature data. Furthermore, the material cards derived from tensile and shear tests for early and late wood using the optimization tool LS-OPT [1] are provided in Fig. 7.

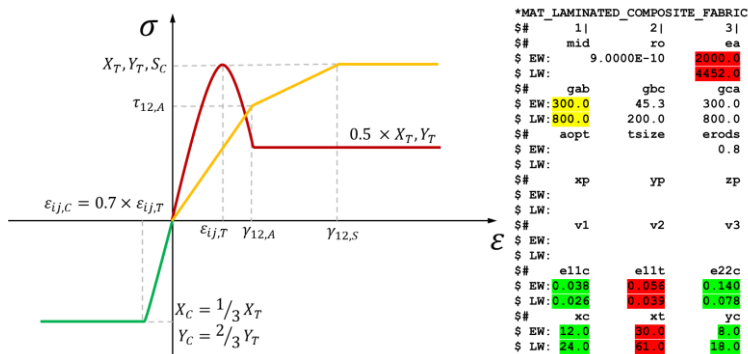


Fig. 7: General behavior of **\*MAT\_058** under tensile and compressive loading (left) and the parameters derived for early wood (EW) and late wood (LW) by numerical calibration (right).

Parameters for shear behavior are highlighted in yellow, parameters related to the tensile behavior are highlighted in red, and compressive parameters are highlighted in green. To account for the remaining load-carrying capacity after failure in one of the loading directions, the SLIMx values were set to 0.5 in the tensile direction, reducing remaining stresses to 50% until final rupture is initiated when the maximum effective failure strain of 80% is reached, assuming that the material is volume preserving [4]. In shear and compressive loading direction, stresses are kept at a constant level. To allow for the definition of a non-linear shear behavior based on the parameters  $\tau_{12,A}$  ( $\tau_{12,A}$ ),  $\gamma_{12,A}$  ( $\gamma_{12,A}$ ),  $S_C$  ( $s_c$ ), and  $\gamma_{12,S}$  ( $g_{ms}$ ), a faceted failure surface based on maximum strengths is chosen by setting  $FS = -1$ . Parameters not listed for the late wood (LW) material card correspond to those provided for the early wood (EW) material card. Based on the experimental results published in [13] and [14], compressive

strength values were estimated as two thirds of the tensile strength in the direction perpendicular to the fibers. Compressive strength in the direction of the fibers was scaled by a factor of one third. Corresponding compressive failure strains were estimated by multiplying the tensile failure strains by a factor of 0.7. These data were also published in [2]. Results of the material calibration for tensile and shear specimens are shown in Fig. 8, also indicating the mean-square error (MSE) in comparison to the experiment. Overall, a very good agreement between simulation and experiment can be found using **\*MAT\_058**.

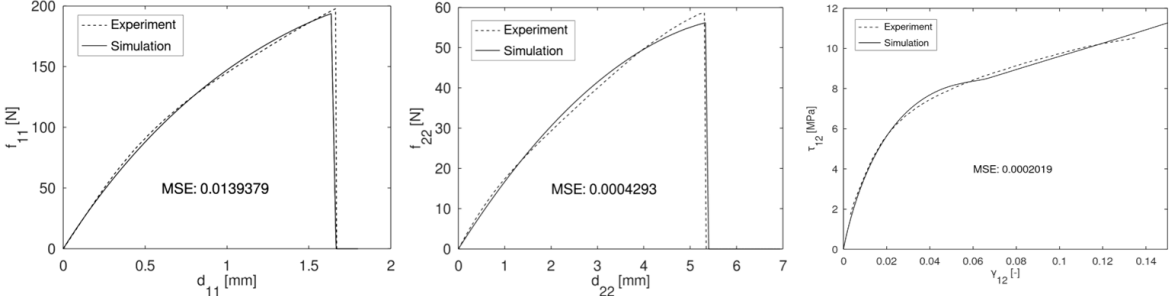


Fig. 8: Results of the material calibration for tensile specimen loaded in fiber (l) and perpendicular to the fiber direction (m) as force-displacement curves. The result for the shear parameter calibration is provided as stress-strain curve (r).

A qualitative evaluation can also be made by comparing the results of the Nakajima test. Fig. 9 illustrates this for a specimen with a web width of 30 mm. Strain concentration is clearly visible in the areas of the early wood (green), where the final failure also occurs. In general, it can be stated that the Nakajima simulations underestimated the possible path of the stamp compared to experiments. Nevertheless, crack path estimation seems to be reasonable when comparing the crack pattern observed in the full-circle Nakajima test and a test with a web width of 125 mm. For the latter, one can clearly see the crack in the center as well as initial failure occurring at the corners of the investigated area.

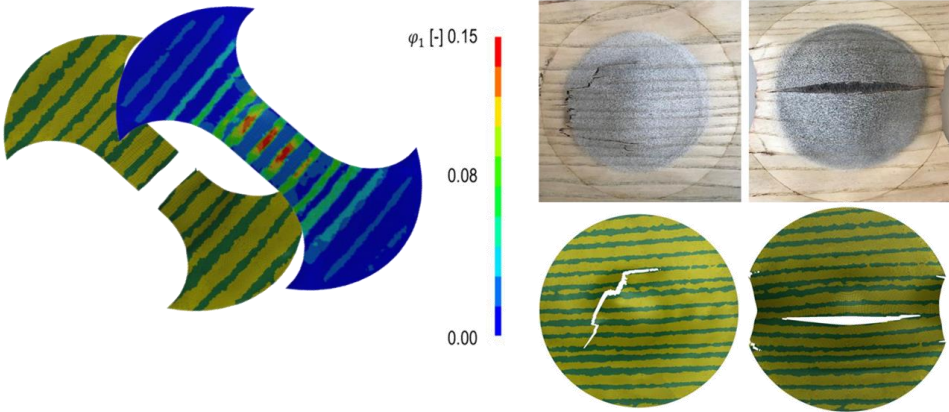


Fig. 9 Illustration of the Nakajima test simulation results showing failure and strain concentration for a web width of 30 mm (left) and qualitative investigation of the crack pattern for the Nakajima test and a test with a web width of 125 mm (right).

### 4.3 Investigation of the scatter of numerical and mechanical properties

Since materials used in automotive industry must not exhibit large scatter in their engineering properties especially when it comes to crashworthiness, the distribution of maximum strength and corresponding failure strains for longitudinal and transverse tensile specimen were investigated. In this context, the numerical simulation should be capable to provide a comparable scatter of the result data considering early and late wood areas through the above-described gray-scale mapping method. Fig. 10 illustrates that the probability density function  $P(x)$  assuming a normal distribution yields comparable results for the maximum stress distribution in both fiber and transverse direction. The prediction of the failure strain distribution especially in the longitudinal direction provides a lower range of variation, which might be due to the collection of the samples from two veneer laminate sheets with slightly different material properties. The variables of the density function are defined as  $x$ , the random variable,  $\mu$ , the mean value and  $\sigma_x^2$ , the variance. The simulation results of the samples are also shown in Fig. 10, indicating different points of failure depending on the early and late wood distribution.

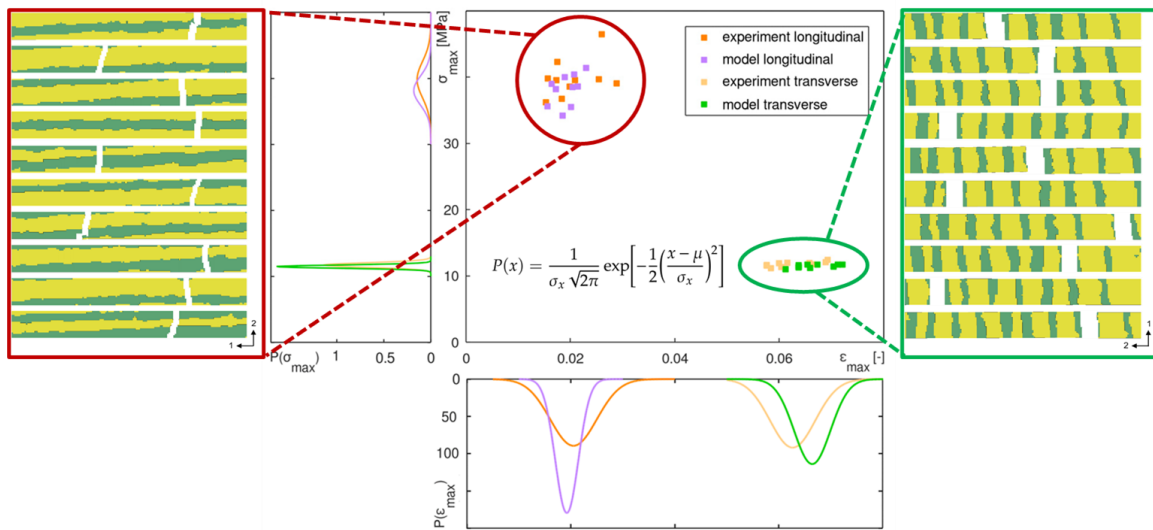
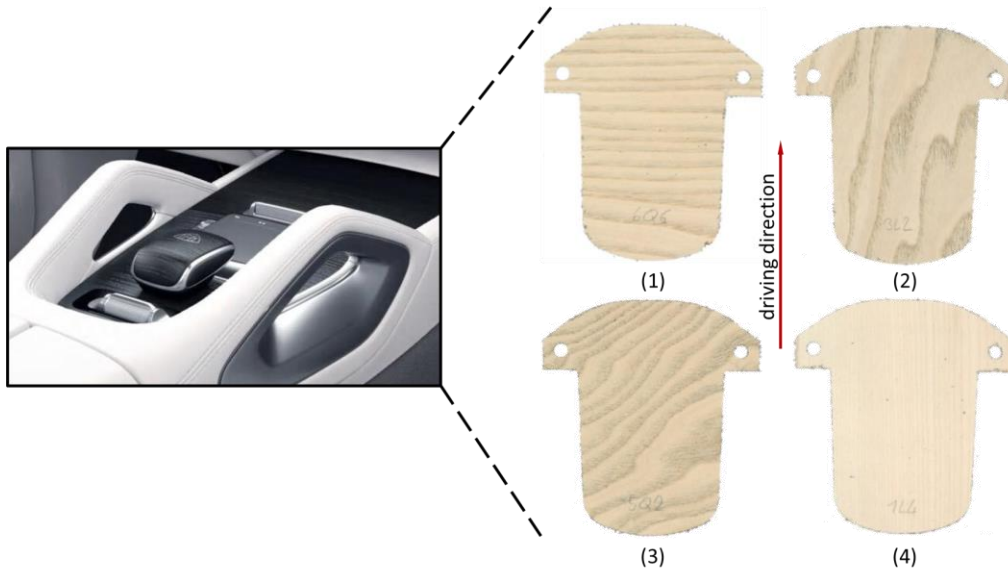


Fig. 10: Distribution of experimentally measured and numerically simulated maximum strengths and strains of wood samples under tensile loading in longitudinal (left) and transversal direction (right).

## 5 Evaluation of the proposed modeling approach

The above-described simulation method was evaluated on the example of a palm rest of the Mercedes-Benz X167 (see Fig. 11). A total of 3 different veneer laminate specimens was investigated with different fiber orientations and various early and late wood distributions. In addition, one sample was made from maple wood veneer laminate to demonstrate the transferability of the proposed modeling technique. For the latter, a different material card was calibrated. Fig. 11 shows a selection of specimens aligned in 0°, 45°, and 90° with the vehicles driving direction and the maple wood sample, which are discussed in the following. The size of each specimen is about 107 x 116 mm<sup>2</sup> and two holes shall keep the specimen in place during the forming process. The process itself is split into two steps: gravity simulation after placing the specimen into its position, and the actual forming process, which takes place at tool-temperatures of 140°C.



*Fig. 11: Illustration of the palm rest used for evaluation purposes and selected specimens with main fiber direction perpendicular to the driving direction (1), aligned with the driving direction (2), 45° to the driving direction (3) and the maple wood specimen (4).*

### 5.1 Step 1: Gravity loading

For the gravity load step, specimens were meshed using quadrilateral, fully integrated shell elements (ETYP=16) with a mesh size of 0.5 mm. The implicit solver of LS-DYNA was used for this calculation step, and the gravity load was applied using `*LOAD_BODY_Z`. A total time of 1.5 s was considered. A mortar contact formulation was used between the edges of the holes and the pins holding the specimen in place. A standard surface-to-surface contact was applied between specimen and die. A visual comparison of the experimental test and the simulation result was performed and showed satisfying results, see Fig. 12.

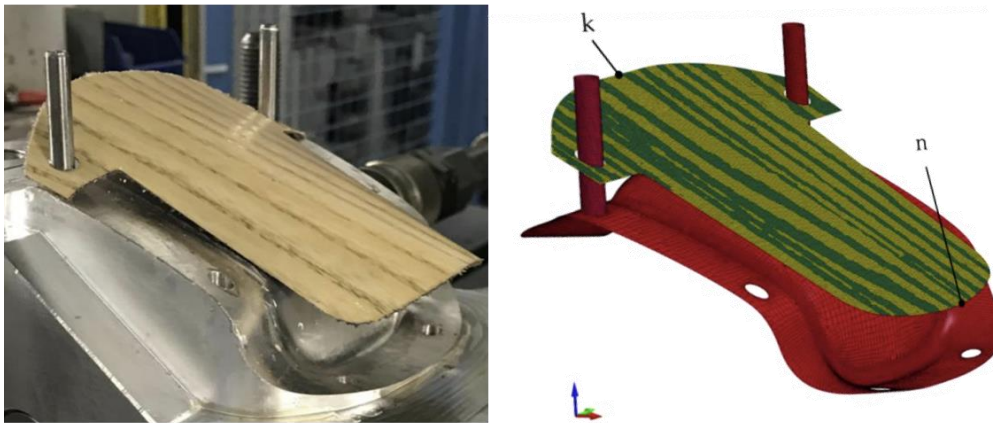


Fig. 12: Comparison of the gravity simulation result (right) with the specimen placed into the forming tool (left).

## 5.2 Step 2: Forming simulation

The forming simulation was performed based on the result mesh of the previous gravity load step. The rigid punch travels 31 mm, and an additional surface-to-surface contact is defined between punch and specimen. The effective failure strain criterion (ERODS) was removed for this simulation step. The simulation termination time was set to 0.1 s, and mass scaling was used to speed-up the analysis. The results are discussed in the following section.

## 5.3 Discussion of the results

The results of the forming experiments and the simulation of the specimens shown in Fig. 11 are presented in Fig. 13. For all specimens, early and late wood zones could be identified clearly, except for the maple wood veneer laminate, where the representation using only one material card proved to be sufficient. All investigated specimens developed wrinkles along the edges or in the corners and at the holes used for holding the specimen in place during the forming process. Those wrinkles are also observed in the simulation and can be investigated visually looking at the resulting deformation. Furthermore, strain concentrations are visible in the fringe plots of the effective strain, indicating that strain concentration is again observed in the early wood zones, which can be explained by the material properties of the wood specimen described previously. It is concluded that the proposed modeling technique is sufficient to predict wrinkles and the formability of veneer laminates.

## 6 Conclusion and outlook

A novel approach to consider early and late wood areas in the forming simulation of veneer laminates based on a gray-scale mapping algorithm implemented in Envyo is presented. Testing procedures for the chosen material model **\*MAT\_LAMINATED\_COMPOSITE\_FABRIC (\*MAT\_58)** for wood specimens are provided and unknown properties are derived from a literature review. The resulting material card for an ash wood veneer laminate is provided. The capability of the presented methods to consider the stochastic distribution observed in experiments is investigated. This is an important step towards the development of a digital twin for veneer laminates and an automated model setup allowing for an investigation of the influence of the locally varying properties of wood. In a final step, the proposed modeling scheme is evaluated using the example of a palm rest from a real interior component of a vehicle.

Further research should concentrate on the automation of the applied techniques, also focusing on the definition of constant lighting conditions when scanning and digitalizing the specimens. Additional research regarding the stochastic distribution of wood material properties in general is necessary, especially if the material is for used for crash-worthiness applications in automotive engineering. On the

mapping side, a proper consideration of the wood fibers interpolated from splines derived from the edges of early and late wood zones could enhance Envyo's mapping capabilities.

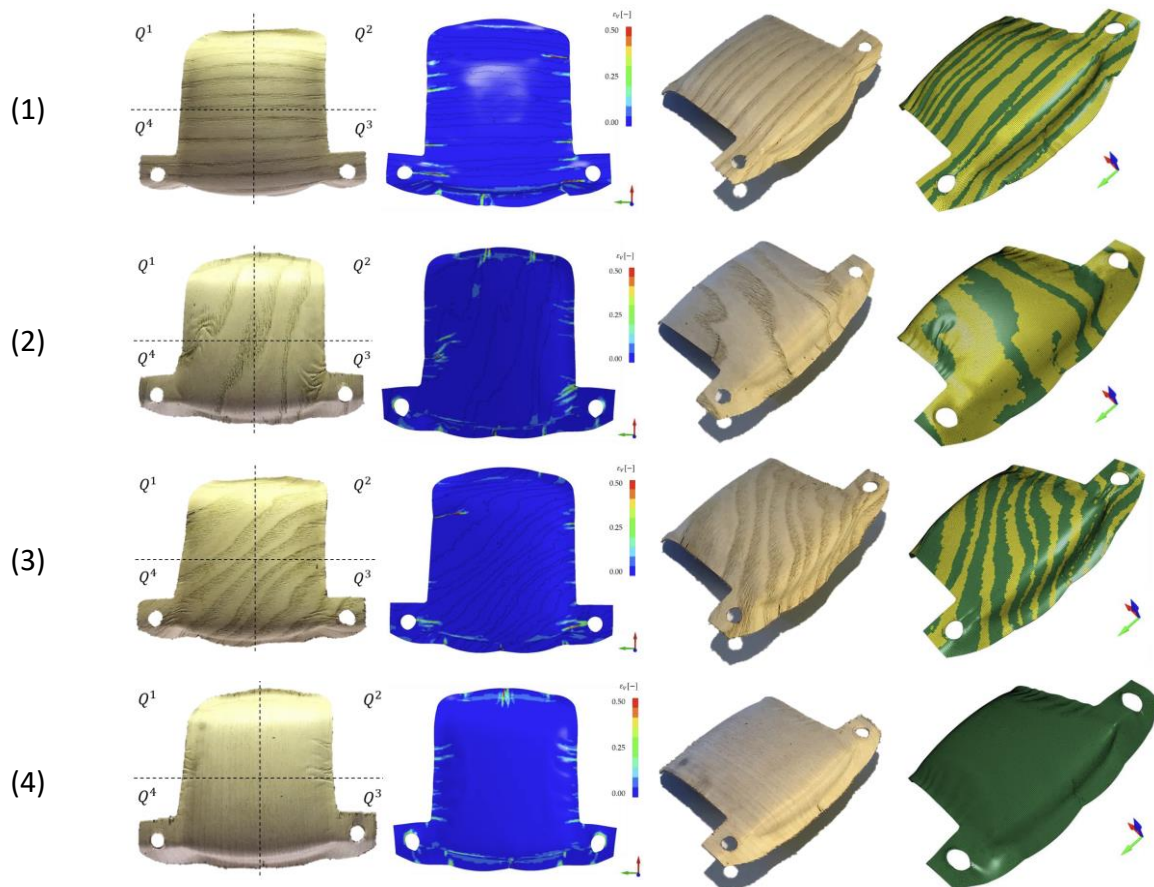


Fig. 13: Comparison between experimental forming result (left, middle-right), and forming simulation result, showing effective strain (middle-left) and the early and late wood zone patterns for these specimens (right).

## 7 Literature

- [1] Zerbst, D., Liebold, C., Gereke, T., Clauß, S., Cherif, C.: "Modelling inhomogeneities of veneers with a grayscale mapping approach", ECCOMAS CompWood, 2019.
- [2] Zerbst, D., Liebold, C., Gereke, T., Clauß, S., Cherif, C.: "Numerical Simulation of the Forming Process of Veneer Laminates", J. Compos. Sci., 2021, 5, 150. <https://doi.org/10.3390/jcs5060150>
- [3] Zerbst, D., Liebold, C., Gereke, T., Haufe, A., Clauß, S., Cherif, C.: "Modelling Inhomogeneity of Veneer Laminates with a Finite Element Mapping Method Based on Arbitrary Grayscale Images", Materials, 2020, 13, 2993. <https://doi.org/10.3390/ma13132993>
- [4] Livermore Software Technology (LST), an ANSYS Company: "LS-DYNA User's Manual, Vol. II – Material Models", 2020.
- [5] DYNAmore GmbH, "Envyo® User's Manual", GER, 2021.
- [6] <https://www.jahn-furniere.de/furnierherstellung.html>
- [7] Zerbst, D., Affronti, E., Gereke, T., Buchelt, B., Clauß, S., Merklein, M., Cherif, C.: "Experimental analysis of the forming behavior of ash wood veneer with non-woven backings" Eur. J. Wood Prod., 2020, 65, 107.
- [8] Buchelt, B., Wagenführ, A.: "Influence of the adhesive layer on the mechanical properties of thin veneer-based composite materials", Eur. J. Wood Prod. 2010, 68, 475-477.
- [9] Krüger, R., Buchelt, B., Wagenführ, A.: "New method for determination of shear properties of wood", Wood Sci. Technology, 2018, 52(6): 1555-1568.

- [10] DIN EN ISO 12004-2:2009-02, Metallische Werkstoffe – Bleche und Bänder – Bestimmung der Grenzformänderungskurve – Teil 2: Bestimmung von Grenzformänderungskurven im Labor (ISO 12004-2:2008), Deutsche Fassung EN ISO 12004-2:2008. Beuth Verlag GmbH, Berlin.
- [11] Matzenmiller, A., Lubliner, J., Tailor, R. L.: “A constitutive model for anisotropic damage in fiber-composites”, *Mech. Mater.* 1995, 20, 125-152.
- [12] Schweizerhof, K., Weimar, K., Münz, T., Rottner, T.: “Crashworthiness analysis with enhanced composite material models in LS-DYNA – merits and limits”, *LS-DYNA World Conference*, Detroit, MI, USA, 21 – 22 Sept. 1998, pp. 1-17.
- [13] Niemz, P., Sonderegger, W.U.: “Holzphysik: Physik des Holzes und der Holzwerkstoffe“; Carl Hanser Verlag GmbH & Company KG: Munich, Germany, 2018; ISBN 9783446457218.
- [14] Ozyhar, T., Hering, S., Niemz, P.: “Moisture-dependent orthotropic tension-compression asymmetry of wood”, *Holzforschung* 2013, 67, 395–404.
- [15] Liebold, C., Zerbst, D., Hedwig, M., Hagmann, S.: “Bake-Hardening effects arbitrary image data and finite pointset analysis results mad accessible with Envyo”, *12<sup>th</sup> European LS-DYNA Conference*, 2019, Koblenz, GER.